Diagnostic Model and Analysis of the Surface Currents in the Tropical Pacific Ocean

Fabrice Bonjean and Gary S.E. Lagerloef

Earth And Space Research, Seattle, U.S.A.

Accepted for publication in

Journal of Physical Oceanography

March 2002

Address:

Fabrice Bonjean

Earth & Space Research

1910 Fairview Ave. E, Suite 102

Seattle, WA 98102

USA

Phone: 206-726-0501; Fax: 206-726-0524

E-mail: bonjean@esr.org

Abstract

A diagnostic model of the tropical circulation over the $0-30\,m$ layer is derived by using quasi linear and steady physics. The horizontal velocity is directly estimated from sea surface height (TOPEX/POSEIDON), surface vector wind (SSM/I) and sea surface temperature (AVHRR + *in situ* measurements). The absolute velocity is completed using the mean dynamic height inferred from the World Ocean Atlas (WOA). The central issue investigated in this study is the more accurate estimate of equatorial surface currents relative to our prior satellite-derived method. The model formulation combines geostrophic, Ekman and Stommel shear dynamics, and a complementary term from surface buoyancy gradient. The field is compared to velocity observations from $15\,m$-depth buoy drifter and equatorial TAO currentmeters. Correlations with TAO data on the equator are much higher in the eastern Pacific cold tongue than before. The mean field in the cold tongue is also much more accurate, now showing the equatorial minimum that splits the south equatorial current into northern and southern branches. The mean current strength is somewhat less than in drifter composites because the mean dynamic topography from WOA remains too smooth. However the seasonal cycle and interannual variations are robust, especially anomalies on the order of $1\,m/s$ during the 1997-98 ENSO. This direct method using satellite measurements provides surface current analyses for numerous research and operational applications.

1 Introduction

Surface currents in the tropical Pacific play an important part in various geophysical phenomena such as the transport of heat (e.g. Picaut et al. 1996, Bonjean 2001) and salt (e.g. Delcroix and Picaut 1998). Monitoring their variations is therefore crucial for climate studies. An analysis of the surface velocity during the 1992 to 1999 period using satellite altimetry and vector wind data was undertaken by Lagerloef et al. (1999) (hereafter *LMLN*). The surface layer velocity $\boldsymbol{U}$ was decomposed into two components, a geostrophic term estimated from the sea surface height (ssh) and a simplified Ekman term from the surface wind-stress ($\boldsymbol{\tau}$). The model was calibrated using velocity observations from lagrangian drifter records. It was apt to describe the broad scale current anomalies, but several discrepancies were revealed from comparison of $\boldsymbol{U}$ to the Tropical Ocean-Atmosphere (TAO) current meter data (*LMLN*, conclusion). Firstly, a westward systematic bias of the analyzed currents ($0.3 - 0.4\, m/s$) was found in the cold-tongue (140^oW, 110^oW). Secondly, the correlation with the TAO measurements was lower at the eastern locations, compared to those at the central and western locations (170^oW, 165^oE). Subsequent comparisons with mean velocity fields derived from buoy drifter and current-meter records (Reverdin et al. 1994, Johnson 2001) show that the diagnostic velocity did not reproduce important details of the near equatorial mean current, namely the two branches of the south equatorial current (SEC) with a minimum of the westward zonal current on the equator. These differences in the cold tongue were mainly attributed to the vertical shear in the shallower equatorial undercurrent (EUC), that was not taken into account by the *LMLN* model.

A motivation of the present study is to solve these problems of estimating satellite derived near-surface velocity in the equatorial area, and in particular in the cold-tongue where thermal changes and vertical shear are important. Therefore, a large part is dedicated to improve the diagnostic model of the surface currents, and we are led to formulation and method that differ from *LMLN* in several respects. The horizontal currents are estimated from the new formulation within an ocean surface layer, using the three surface variables

ssh, $\boldsymbol{\tau}$, and sea surface temperature (*sst*). These three variables are monitored in global extent through satellite remote sensing (+ *in situ* measurements for *sst*). The mean *ssh*, which estimate will soon be improved from satellite gravity measurements, is here equal to the mean dynamic height (*dh*) derived from the World Ocean Atlas (WOA). The estimated currents are validated with independent velocity observations based on drifter records in the basin and on current data at the four equatorial TAO moorings.

2 Data

Most of the satellite and *in situ* data used in this study were presented in detail by *LMLN*, and a brief summary is given here. The diagnostic observational fields are directly used to estimate the near-surface velocity, and the *in situ* reference velocity data utilized for validation. The period here examined goes from October 1992 to July 2000.

2.1 Diagnostic fields

Alongtrack altimeter sea level data from Topex/Poseidon were interpolated by objective analysis on a $1^o \times 1^o$ grid within $25^oN - 25^oS$ and $120^oE - 70^oW$, and with a temporal sample interval of about 10 days ($36\, yr^{-1}$) (Lagerloef et al. 1999). Because of geoid uncertainty, only departure from temporal mean is considered. The variational analysis Special Sensor Microwave Imager (SSMI) winds (Atlas et al., 1996) are used to compute the surface wind stress vectors using the drag relationship established by Large and Pond (1981). The global satellite + *in situ sst* field of Reynolds and Smith (1994) is subsampled over the same time grid as the data above. The mean *dh* relative to 1000 *dbar* was derived from the analyzed *in situ* temperature and salinity of Levitus et al. (1994) and Levitus and Boyer (1994) (WOA), on the same grid as the above fields. It is added as a mean datum to *ssh*, and the mean circulation map shown hereafter is based, for the geostrophic current part, on this mean field.

2.2 Reference data for validation

The seasonal fluctuations from Reverdin et al. (1994) and based on 15 m-depth buoy drifters and currentmeters (hereafter *DRCM* for DRifters and CurrentMeters) are examined for comparison with the derived velocity seasonal cycle. More recent mean surface currents from drifter records analyzed by Johnson (2001) are also used for adjustment and comparison. Measurements over the past 20 years (1979 to mid-1999) are included in the Johnson (2001) analysis, and therefore the data distribution is more complete than that of the *DRCM* field. This provides for improved signal-to-noise ratio, particularly for the meridional component. The 10 m-depth horizontal current data from the four equatorial TAO moorings (NOAA PMEL; R. Weisberg, University of Southern Florida) are averaged in $\simeq$10-day periods coinciding with the satellite data time grid. Except at 170^oW where only ADCP data are used, the time series are built from current-meter measurements, sometimes completed with ADCP data.

3 Model

3.1 Diagnostic equations and solutions

We consider a quasi linear and steady flow in a surface layer where the horizontal velocity $\boldsymbol{U} \equiv (u, v)$ is allowed to vary with vertical coordinate z, and where vertical turbulent mixing is characterized by an eddy viscosity A uniform with depth. The vertical shear $\boldsymbol{U}' \equiv \boldsymbol{U}_z$ reaches zero at a constant scaling depth $z = -H$. A simplified buoyancy force θ, solely function of sst, is retained in the vertical hydrostatic balance. Writing in complex notation

$\boldsymbol{U}(x,y,z,t) \equiv u + iv$ and $\boldsymbol{\nabla} \equiv \partial/\partial x + i\partial/\partial y$, the basic equations are

$$if\boldsymbol{U} = -\frac{1}{\rho_m}\boldsymbol{\nabla} p + A\boldsymbol{U}'_z \tag{1a}$$

$$\frac{1}{\rho_m} p_z = -g + \theta \tag{1b}$$

$$\boldsymbol{\nabla}\theta = g\chi_T \boldsymbol{\nabla} sst, \tag{1c}$$

with $-H \leq z \leq 0$, and subject to the following boundary conditions:

$$\boldsymbol{U}'(z=0) = \boldsymbol{\tau}/A \tag{2a}$$

$$\boldsymbol{U}'(z=-H) = 0 \tag{2b}$$

The characteristic density is $\rho_m = 1025\, kg/m^3$, the gravity acceleration $g = 9.8\, m/s^2$ and the coefficient of thermal expansion $\chi_T \approx 3 \times 10^{-4}\, K^{-1}$. The vector field $\boldsymbol{\tau} = \tau^x + i\tau^y$ represents the surface wind stress divided by ρ_m. The independent model parameters H and A are determined in subsequent sections: A is parameterized in function of surface wind magnitude (Sec. 3.2), and H adjusted as a constant depth scale using observations (Sec. 3.3).

Hereafter the variable ζ denotes the displacement of the ocean-atmosphere interface, and is known from dh + de-meaned ssh. From Eqs (1) we derive the formulation of the velocity averaged between the interface and an arbitrary depth $h < H$. After simplifications implied by $\left|\frac{\theta}{g}\right| \ll 1$, we have

$$if\overline{\boldsymbol{U}} \equiv \frac{if}{h}\int_{-h}^{0} \boldsymbol{U}(z)dz = -g\boldsymbol{\nabla}\zeta + \frac{h}{2}\boldsymbol{\nabla}\theta + \frac{\boldsymbol{\tau} - A\boldsymbol{U}'(-h)}{h} \tag{3}$$

In (3), the term $-g\boldsymbol{\nabla}\zeta$ mainly represents the pressure-gradient force (per mass unit), with an additional contribution $\frac{h}{2}\boldsymbol{\nabla}\theta$ from buoyancy gradient. The term $\frac{\boldsymbol{\tau}-A\boldsymbol{U}'(-h)}{h}$ is the net drag force from vertical diffusion applied to the layer of thickness h. As we see later in Sec. 3.1.1, the net drag force depends on both $\boldsymbol{\tau}$ and $\boldsymbol{\nabla}\theta$. For comparison, *LMLN* considered equation (3) with $\boldsymbol{\nabla}\theta = 0$, and replaced $A\boldsymbol{U}'(-h)$ by a Rayleigh-friction term $r\boldsymbol{U}_e$, where $\boldsymbol{U}_e$ denotes the ageostrophic layer-velocity and r a constant drag coefficient. The present formulation and *LMLN* are equivalent if correspondence $A \leftrightarrow \frac{rh}{2}$ and $\boldsymbol{U}'(-h) \leftrightarrow \frac{2\boldsymbol{U}_e}{h}$ is satisfied.

From *LMLN*, $\frac{rh}{2} = 3.5 \times 10^{-3} m^2/s$, and is on the order of A (Santiago-Mandujano and Firing, 1990). However, the parameter A varies here in time and location as we assume this mixing parameter is governed by the local surface wind speed, consistent with Santiago-Mandujano and Firing (1990) (Sec. 3.2 here). A standpoint of the *LMLN* formulation is that the ageostrophic velocity vanishes at the layer bottom. Under this condition, the relationship $\boldsymbol{U}'(-h) = \frac{2\boldsymbol{U}_e}{h}$ is verified only if $\boldsymbol{U}'$ is uniform over the layer. Since the present formulation implies that $\boldsymbol{U}'$ depends on z (otherwise there would be no drag force), it constitutes a higher order turbulence-closure parameterization than *LMLN*. Significant differences between the two formulations are found within the equatorial area, where the present formulation accounts for a large part of the mean bias reduction with respect to *in situ* current observations (Sec. 4.1).

For consistency with *LMLN*, we estimate $\overline{\boldsymbol{U}} \equiv \frac{1}{h}\int_{-h}^{0} \boldsymbol{U}(z)dz$ for $h = 30\,m$. It is function of the variables and parameters previously introduced, and it is known from (3) since the bottom shear $\boldsymbol{U}'(-h)$ is next determined (Sec. 3.1.1). However, its analytical expression is rather complicated, and we only present the formulations of $\boldsymbol{U}'(z)$ and velocity $\boldsymbol{U}_0$ at $z = 0$, seeing that

$$\overline{\boldsymbol{U}} = \boldsymbol{U}_0 + \frac{1}{h}\int_{-h}^{0}\int_{0}^{z} \boldsymbol{U}'(Z)\,dZ\,dz \tag{4}$$

For practical purpose, (4) is also better suited than (3), since it isolates the problem of equatorial singularity in the formulation of $\boldsymbol{U}_0$ (single level $z = 0$). Indeed, the last term in r.h.s of (4), which accounts for layer-velocity contribution, is regular everywhere including $y = 0$ (Secs. 3.1.1 and 3.1.2).

3.1.1 Vertical shear

The equation of the velocity shear is obtained by differentiating (1a) with respect to z and by using (1b):

$$\boldsymbol{U}'_{zz} - \frac{if}{A}\boldsymbol{U}' = \frac{1}{A}\boldsymbol{\nabla}\theta \tag{5}$$

Eq. (5) is a 2nd-order differential equation of the unknown $\boldsymbol{U}'$ and is subject to the boundary conditions (2a) and (2b). When the vertical momentum diffusion is neglected ($A \to 0$), Eq. (5) reverts to the classic thermal wind equation $f\boldsymbol{U}' = i\boldsymbol{\nabla}\theta$. If $\boldsymbol{\tau}$, $\boldsymbol{\nabla}\theta$, A ($\neq 0$) and H are known, $\boldsymbol{U}'$ is determined by

$$\boldsymbol{U}'(z) = \overbrace{\frac{\sinh\left(\frac{H+z}{\hbar_e}\right)}{\sinh\left(\frac{H}{\hbar_e}\right)}\frac{\boldsymbol{\tau}}{A}}^{\boldsymbol{U}'_\tau} + \overbrace{\frac{2\sinh\left(\frac{H+z}{2\hbar_e}\right)\sinh\left(\frac{z}{2\hbar_e}\right)}{\cosh\left(\frac{H}{2\hbar_e}\right)}\frac{\hbar_e^2\boldsymbol{\nabla}\theta}{A}}^{\boldsymbol{U}'_\theta} \tag{6}$$

where $\hbar_e \equiv \left(\frac{A}{if}\right)^{1/2}$ is complex and its modulus proportional to the Ekman depth $h_e \equiv \sqrt{2A/|f|} = \sqrt{2}|\hbar_e|$. The term $\boldsymbol{U}'_\tau$ is a shear contribution from wind stress and $\boldsymbol{U}'_\theta$ from horizontal buoyancy gradient. $\boldsymbol{U}'$ is defined everywhere, including the equator where $h_e \to \infty$, and this is also true of the successive vertical integrations of $\boldsymbol{U}'$ in r.h.s of (4).

3.1.2 Surface velocity

In (3), the expression of net drag force $\frac{\boldsymbol{\tau} - A\boldsymbol{U}'(-h)}{h}$ is known from (6). Assuming for the time being that h is a moving variable, and letting h tend toward zero, we combine (3) and (6) to obtain the following new equation of the velocity at the surface:

$$if\boldsymbol{U}_0 = -g\boldsymbol{\nabla}\zeta + \frac{1}{H}\boldsymbol{q}(\frac{H}{\hbar_e})\boldsymbol{\tau} + \frac{H/2}{\boldsymbol{q}(\frac{H}{2\hbar_e})}\boldsymbol{\nabla}\theta, \tag{7}$$

where $\boldsymbol{q}(\xi) \equiv \frac{\xi}{\tanh(\xi)} = 1 + \frac{\xi^2}{3} - \frac{\xi^4}{45} + \cdots$. The direct solution $\boldsymbol{U}_0$ of (7) is singular for $f = 0$ if the r.h.s is not zero on the equator (discussed in Sec. 3.1.3). Aside from this, Eq. (7) defines $\boldsymbol{U}_0$ as the summation of three terms linearly related to $\boldsymbol{\nabla}\zeta$ ($\boldsymbol{U}_\zeta$), $\boldsymbol{\tau}$ ($\boldsymbol{U}_{\tau 0}$) and $\boldsymbol{\nabla}\theta$ ($\boldsymbol{U}_{\theta 0}$) respectively, and function of the two parameters A and H. The term $\boldsymbol{U}_{\tau 0}$ is different from the classic Ekman velocity and from the *LMLN*-Ekman term, and is described in Appendix B.1.

The layer velocity $\overline{\boldsymbol{U}}$ is deduced from (4), and likewise $\boldsymbol{U}_0$, is the sum of three terms derived from $\boldsymbol{\nabla}\zeta$ ($\boldsymbol{U}_\zeta$), $\boldsymbol{\tau}$ ($\overline{\boldsymbol{U}_\tau}$) and $\boldsymbol{\nabla}\theta$ ($\overline{\boldsymbol{U}_\theta}$). The velocity results presented in section 4 are based on this formulation without any further simplification.

3.1.3 Equatorial limit case, $f \to 0$

A necessary balance condition for estimating the surface current on the equator is imposed by setting $f = 0$ ($h_e \to \infty$) in (7). Using $\boldsymbol{q}(0) = 1$ we have

$$-g(\boldsymbol{\nabla}\zeta)_E + \frac{\boldsymbol{\tau}_E}{H} + \frac{H(\boldsymbol{\nabla}\theta)_E}{2} = 0, \tag{8}$$

where the subscript E denotes the equatorial value at $y = 0$. Eq. (8) requires that the pressure gradient force (from $\boldsymbol{\nabla}\zeta$ and $\boldsymbol{\nabla}\theta$) and the wind-stress term must compensate for each other on the equator. Using the observed data, this momentum balance is later examined in order to calculate the depth scale H, sole parameter in (8) (Sec. 3.3). Because of measurement uncertainty and missing momentum terms, the exact balance (8) is not expected to be satisfied at all longitude and time. Thus Eq. (7) can be singular for $f = 0$, and requires a special treatment (Sec. 3.4).

Assuming (8), it is instructive to write the equatorial velocity considering the development of (7) around $y = 0$ and limiting the expansion to first order. Using Taylor development of $\boldsymbol{q}(\xi)$, $f = \beta y$, and neglecting $(\boldsymbol{\tau}_y)_E$ and $(A_y)_E$ we have

$$(\boldsymbol{U}_0)_E = \underbrace{\frac{ig[(\boldsymbol{\nabla}\zeta)_y]_E}{\beta}}_{\text{I}} + \underbrace{\frac{H\boldsymbol{\tau}_E}{3A_E}}_{\text{II}} - \underbrace{\frac{iH[(\boldsymbol{\nabla}\theta)_y]_E}{2\beta}}_{\text{III}} - \underbrace{\frac{H^3(\boldsymbol{\nabla}\theta)_E}{24A_E}}_{\text{IV}} \tag{9}$$

From (9) the contributions to the equatorial velocity are therefore: (I) the classic equatorial "geostrophic" velocity, proportional to 2nd-order derivatives of the surface height, (II) a downwind term proportional to wind stress. (III) is proportional to 2nd-order derivatives of θ, analogous to (I) with $\boldsymbol{\nabla}\zeta \leftrightarrow \frac{-H\boldsymbol{\nabla}\theta}{2g}$, and (IV) proportional to (minus) the buoyancy gradient, analogous to (II) with $\boldsymbol{\tau} \leftrightarrow \frac{-H^2\boldsymbol{\nabla}\theta}{8}$. Note the formulation (9) is not directly considered to calculate $\boldsymbol{U}_0$, but is implicitly satisfied by the surface velocity hereafter estimated.

3.2 Turbulent viscosity A

Former studies revealed that the coefficient A is not uniform and may directly depend on the local surface wind velocity. Using in situ velocity and wind speed data between 3^oN and 3^oS

in the central Pacific, Santiago-Mandujano and Firing (1990) found with good confidence that A is proportional to the square of the wind speed ($|W|^2$), confirming much earlier studies by Ekman. Using the lagrangian drifter data set in the tropical pacific between 1987 and 1994, Ralph and Niiler (1999) tested several models of the wind-driven currents beyond the close-equatorial zone ($3^oN - 3^oS$). They found that when A is proportional to $|W|^2$ the classic Ekman model explains a significantly larger fraction of the ageostrophic velocity variance than that obtained when A is uniform. They also tested a more complex parameterization of A accounting for the upper-ocean stratification, and in that case their model only explained a slightly larger fraction of the variance.

These studies indicate that the simple assumption $A \propto |W|^2$ is appropriate and we apply the empirical formulation determined by Santiago-Mandujano and Firing (1990),

$$A = a(|W|/W_1)^b, |W| \geq 1\,m/s, \tag{10}$$

where $W_1 = 1\,m/s$, $a = 8 \times 10^{-5}\,m^2/s$ and $b = 2.2$. In the rare case when $|W| < 1\,m/s$, A is set to the constant a, implying that diffusion is slightly active even in weak wind conditions.

3.3 Depth-scale H

In this section, we evaluate H and justify the assumption that it is constant in our model. H is implied by Eq. (2b), and thus is *a priori* on the scale of the EUC core depth on the equator ($\simeq 100\,m$). An additional constraint on H is that $\boldsymbol{\nabla}\theta$ is vertically uniform and approximated by its surface value for $-H \leq z \leq 0$ (Eq. 1c). The latter condition requires H to be on the order of the mixed-layer depth h_{mix}, which maximum value in the tropical Pacific is $70 - 80\,m$ (e.g. Bonjean 2001). Therefore, the optimal constant H must be chosen small enough to stay close to h_{mix} and large enough to satisfy (2b).

The principal condition to infer H on the equator is the dynamic equatorial balance (8), and it is evaluated using mean dh, time-averaged $\boldsymbol{\tau}$ and sst. Another condition (empirical) is that the difference between observed and modeled currents within the basin should be

minimum. This is examined *a posteriori* with a mean drifter velocity field and the TAO current measurements.

3.3.1 Equatorial balance

The parameter H (in $y = 0$) is determined by minimizing the zonal and meridional momentum residuals on the equator:

$$\mathcal{M}^x(x,H) = g(\zeta_x)_E - \frac{H}{2}(\theta_x)_E - \frac{1}{H}(\tau^x)_E \tag{11a}$$

$$\mathcal{M}^y(x,H) = -g(\zeta_y)_E + \frac{H}{2}(\theta_y)_E + \frac{1}{H}(\tau^y)_E \tag{11b}$$

Writing $||\mathcal{M}^i|| = \sqrt{\frac{1}{N_x}\sum_x [\mathcal{M}^i(x,H)]^2}$ as the r.m.s residual compiled zonally, we show in Fig. 1 (top) the derivatives of $||\mathcal{M}^x||$ and $||\mathcal{M}^y||$ with respect to H. Minimum of $||\mathcal{M}^x||$ is reached asymptotically. For $H \geq 70\,m$, both derivatives of $||\mathcal{M}^x||$ and $||\mathcal{M}^y||$ are nearly zero, and the balance (8) is not sensitive to H. Since H must also be close to the mixed-layer depth (as remarked before), the lower limit $H = 70\,m$ is chosen. Note that for increasing H, $||\mathcal{M}^y||$ passes by an exact minimum for $H = 10 - 20\,m$, and after a small overshoot, quickly converges toward zero. We see next paragraph that $H = 10 - 20\,m$ implies unrealistic velocity, and that $H \sim 70\,m$ corresponds to the best adjustment. The momentum balance as a function of longitude for $H = 70\,m$ is shown in Fig. 2. In most of the basin, the surface zonal stress produced by the westward winds is compensated for by the eastward pressure gradient force (top). The northward cross-equatorial wind stress is over-compensated for by the southward pressure gradient force from the central area to the east (bottom).

3.3.2 Control study (whole basin)

We calculate the velocity for H varying from 10 to $100\,m$, using the complete model and method presented later in this section. The mean flow is evaluated from the observations of mean $\boldsymbol{\tau}$, *sst* and *dh* in the tropical Pacific ($20^oN - 20^oS$, $120^oE - 80^oW$). The mean current field derived from drifters (Johnson, 2001) is chosen as the validation reference. Standard

deviation of the difference between modeled and reference velocities (*stdd*) is computed in the spatial domain for each value of H, and its derivative with respect to H is plotted in Fig. 1 (bottom, thick line). A minimum is again asymptotically reached for $H \approx 70 - 80\,m$ ($stdd = 8$ and $3\,cm/s$ for zonal and meridional components respectively). The model is sensitive to H up until $\sim 70\,m$, and becomes insensitive to larger H. For $H \sim 10 - 20\,m$, *stdd* is far from minimum, and indeed, the corresponding velocity maps are quite unrealistic (not shown), dismissing these small values of H. A similar analysis is done at the four equatorial TAO locations (165^oE, 170^oW, 140^oW and 110^oW). The velocity is estimated in function of H using the time-varying *ssh*, $\boldsymbol{\tau}$ and *sst*, and the reference velocity for comparison is the observed $10\,m$-depth current at the TAO moorings. Here *stdd* is calculated in the time domain over the October 1992 to July 2000 period, and the H-derivative is plotted (thin lines). The four curves reach a minimum when H is between 40 and $80\,m$, and in all cases, *stdd* varies slowly in function of H within this range. Hence, $H = 70\,m$ is compatible with the minimizing requirement at the TAO moorings for the time-varying velocity.

From this diagnosis, we conclude it is valid to assume that the depth-scale parameter is uniform and constant, and $H = 70\,m$ is a practical value that satisfies to a reasonable degree both requirements: minimization of equatorial momentum balance residual and minimization of the difference between estimated and observed velocity.

Before leaving this discussion, we give here a final remark. We verified that at all locations including the equator the estimated velocity is quasi-insensitive to variations of H around $\sim 70\,m$ and especially larger H. Considering a depth-scale parameter varying with longitude, latitude or time would thus not significantly alter the results of our diagnostic model, particularly if H increases, as it is expected to do for example in western regions. An apparent reason for this (which is not discussed here) is that sole the near-surface velocity ($0 - 30\,m$) is considered. In contrast, the assumption of a constant H probably becomes unrealistic for velocity estimate at deeper levels.

3.4 Equatorial singularity

Equation (7) (completed by (4)) is the governing formulation for estimating surface currents at all latitudes. To remain valid at $y = 0$, the sum of the terms in r.h.s must be zero on the equator as shown by (8), which we minimized to determine the depth scale H. Because of measurement uncertainty and missing momentum terms, the exact balance is not satisfied in the observed fields, particularly in the meridional direction (Sec. 3.3.1). Therefore there is singularity for $f = 0$, and it is a classic issue arising when estimating velocity from geostrophic relationship and Ekman-like formulation, as in the present study.

The method for estimating the surface velocity $\boldsymbol{U}_0$ across the equator is presented in details in appendix A and we give the main points here. The estimated velocity between $8^o N$ and $8^o S$ is obtained as a linear combination of M orthogonal polynomials, which satisfies Eq. (7) through a weak formulation. The parameter $M = 12$ is adjusted such that on the one hand $\boldsymbol{U}_0$ is identical to the exact solution when there is no singularity, and on the other hand equatorial antisymmetrical features are filtered from the solution when there is a singularity. Beyond the $8^o N - 8^o S$ latitudinal band, the estimated velocity is directly obtained from (7) dividing both l.h.s and r.h.s by $i \times f$ (raw solution). The transition from polynomial solution to raw solution is accomplished within 5^o and 8^o in both hemispheres using a linear weighing function. Since the polynomial-expansion procedure is linear, it is applied separately to each of the three terms in r.h.s of (7), and the three contributions are summed to compose the total velocity.

4 Results

We discuss the near-surface currents over the surface layer of thickness $h = 30\,m$, estimated in the tropical Pacific, from October 1992 to July 2000. The velocity is inferred from de-meaned *ssh* + mean *dh*, $\boldsymbol{\tau}$ and *sst* data. The two parameters are $H = 70\,m$, and A parameterized in function of wind speed as in section 3.2. The method in appendix A is employed to ensure

continuous and regular velocity across the equator.

As we focus on the intra-seasonal to interannual timescales, the velocity is calculated with the 10-day resolution enabled by the satellite data. A mean seasonal cycle is estimated from a simple average procedure over all years in the study, excluding the extreme ENSO period of 1997-1998. The velocity anomalies are obtained by subtracting the mean seasonal cycle from the total velocity field.

4.1 Mean velocity

On overall the estimated mean flow is in close agreement with the drifter velocity (Fig. 3, top two panels). From north to south, north equatorial current (NEC), north equatorial counter current (NECC), and SEC with two branches in the eastern part are reproduced by the diagnostic model. The estimated velocity also displays a realistic poleward drift in both hemispheres. The standard deviation of difference between observed and estimated velocity fields is 8 and $3\,cm/s$ for zonal and meridional components respectively. Hereafter, the velocity meridional structure (from the observations) is described in more details for both zonal and meridional components.

Zonal velocity. The term u_ζ derived from dh has a dominant contribution (Fig. 4 top, right), and explains (in a diagnostic sense) the eastward deflection due to the EUC and the two branches of SEC. The term $\overline{u_\theta}$ has a significant contribution on the equator which partially accounts for the EUC eastward deflection. The wind stress velocity $\overline{u_\tau}$ is important to match the drifter velocity profile on overall, but is smaller than u_ζ in magnitude. Accordingly, the two terms $u_\zeta + \overline{u_\theta}$ representing the long-term adjustment of the surface ocean circulation are dominant compared to the direct wind-driven term $\overline{u_\tau}$.

Interestingly, the mean zonal velocity from the drifter field has an amplitude minimum just south of the equator (1^oS). This is rather well reproduced by the diagnostic model which zonal velocity minimum is located at 1.5^oS (resolution is $(\frac{1}{2})^o$ for the drifter field, 1^o for the diagnostic model). The eastward deflection and its slight offset to the south are fea-

tures coming from u_ζ estimated from dh, and dh has also a local minimum at 1.5^oS in the cold tongue (not shown). As the minimum of $\overline{u}$ likely results from the vertical advection of eastward momentum from the EUC below (Philander and Pacanowski 1980), this clearly suggests that the impact of EUC on surface flow is imprinted on the surface pressure distribution.

Meridional velocity. The term $\overline{v_\tau}$ is the largest in magnitude, and implies the strongest (positive) equatorial divergence. It is for a large part compensated for by $v_\zeta + \overline{v_\theta}$ which is convergent within the equatorial zone.

Significant discrepancy between the derived velocity and the drifter field is evident in the NECC region where the eastward velocity is underestimated, and in the western part where equatorial poleward divergence is too strong (Fig. 3 top panels, and Fig. 4 top-left). Most of the difference may largely be the effect of data error and smoothing of the diagnostic fields, particularly dh. For example, *LMLN* showed that geostrophic currents may be reduced by $30-40\%$ relative to drifters, and this is apparent in Fig. 4 (top-right), considering the contribution of u_ζ compared to the drifter velocity profile in the NECC area. Another indication of the effect of data uncertainty is shown in an additional analysis that we performed using GCM-simulated *ssh*, $\boldsymbol{\tau}$ and *sst* from Seidel and Giese (1999). In contrast to observations, GCM fields are entirely consistent with each other (same time period, same grid...) and the data noise is low. In this GCM, *sst*, TOGA subsurface temperature and de-meaned Topex/Poseidon *ssh* were assimilated, but no velocity data were used for assimilation. As seen in Fig. 3 (bottom two panels), the estimated velocity derived from the GCM fields is nearly identical to the GCM velocity itself, notably in the NECC region.

Comparison with LMLN. In Fig. 4 is also shown the mean velocity derived from the *LMLN* method. Both *LMLN* and the present model agree well from about 3^oN and 3^oS poleward, and are in close agreement with the drifter velocity (left panels). Within the $3^oN - 3^oS$ area the *LMLN* velocity does not reproduce the two branches of the SEC. It usually overestimates the westward velocity on the equator ($30 - 40\, cm/s$), in comparison with both drifter velocity and TAO current data. One principal factor is that the earlier

geostrophic method was based on a smooth weighing function and a regression fit that expressed $\boldsymbol{U}_\zeta$ as a 2nd-order polynomial with respect to latitude between 5^oN and 5^oS. This only preserved a single maximum or minimum across the latitude range and effectively filtered the structures evident in Fig.4. The present approach using the family of orthogonal polynomials recovers these structures accurately. The other factor is that the $LMLN$-Ekman term represents a downwind velocity about 50% larger than $\boldsymbol{U}_\tau$. The higher-order parameterization of vertical momentum diffusion in the present formulation is function of both latitude and depth, and effectively implies a stronger attenuation with depth of the current on the equator (see also Appendix B.2).

4.2 Mean seasonal variations

The estimated seasonal cycle of the currents are shown in Fig. 5 for four representative months. From winter to spring the SEC is strong ($50\,cm/s$), and westward fluctuations are extended from east to west along the equator while the NECC attenuates progressively until April. At the beginning of spring, eastward velocity replaces the westward SEC on the equator in the east ($\simeq 30cm/s$) and these eastward fluctuations propagate toward the west until summer. In the meantime the NECC reappears and strengthens. From early summer to autumn, the SEC again accelerates with westward equatorial flow building from east to west, while the NECC remains intense until the end of the year ($\simeq 30 - 40\,cm/s$). In late autumn the SEC withdraws from the western regions and variable equatorial currents appear from November to January in the warm pool ($\simeq 0 - 40\,cm/s$).

The estimated seasonal velocity is in agreement with the $DRCM$ climatology for the large scales, and here we present the main points of the comparison. Along the equator and throughout the year (Fig. 6, top), the two de-meaned zonal velocities show similar timing and amplitude. Notably, eastward fluctuations in spring ($> 40\,cm/s$) imply reversal of the SEC east of 140^oW, and propagate westward until summer. Intensification of the SEC occurs during summer in the east ($30\,cm/s$) and during late winter-early spring in

the west ($> 20\,cm/s$). Away from the equator the largest fluctuations are located in the northern part of NECC (encompassed within $5^oN - 12^oN$ from west to east), coinciding also with the northernmost position of the intertropical convergence zone (ITCZ). Zonal velocity fluctuations of the two fields are in close agreement (Fig. 6, middle), showing attenuated NECC from winter to summer and intensified current during summer-autumn. The fluctuation amplitudes of the two fields are very similar (maximum $> 15\,cm/s$) compared to mean velocity (Sec. 4.1), indicating that the diagnostic model here applied to the satellite data for the fluctuations only (no mean dh) recovers well the magnitude of the NECC variations. Within that same region ($5^oN - 12^oN$) are also found the largest seasonal fluctuations of the meridional velocity. The two fields show comparable variations (Fig. 6, bottom): northward fluctuations from winter to spring, reversing southward from summer to autumn (maximum $\sim 6\,cm/s$ on average over the latitude band). Close to the equator (not shown), the amplitude of meridional fluctuations is weak ($\sim 1\,cm/s$), and the noise in the drifter field is probably too large to conclude.

On the equator, the largest differences between the two fields are found in the central-western area around January-February ($\sim 30\,cm/s$). Elsewhere and for the other time periods, the differences are less than $10 - 15\,cm/s$. Most of these discrepancies are the result of a systematic time lag occurring mainly in the west, *DRCM* lagging the derived velocity by about 1 month. We note that a similar lag between drifter velocity and TAO mooring current is evident in figures from Yu and McPhaden (1999a) and G. Johnson (personal communication). This may indicate that seasonal variations of equatorial divergence affect the drifter sampling and introduce a slight (seasonal) bias in the *DRCM* field. Another source of discrepancy between derived velocity and *DRCM* is the difference between the two periods relative to each analysis (1987-April 1992 for *DRCM* and 1993-1999 for satellite data). As shown in Frankignoul et al. (1996), interannual variability is large in the equatorial region especially in the west, therefore the estimation of one seasonal-cycle realization substantially depends on the period of analysis. Difference from real seasonal currents may also be related to assumptions of the diagnostic model, in particular the quasi-steady assumption implying

that local acceleration (u_t, v_t) is neglected (see conclusion).

4.3 Total variations and anomalies

4.3.1 Zonal velocity

The estimated velocity is compared to the $10\,m$-depth measurements from currentmeter and ADCP data, at the four equatorial TAO moorings (Fig. 7). Consistent with results in section 4.1, the mean westward bias in the east is much reduced compared to that in *LMLN*: at 140^oW and 110^oW the mean difference $\overline{u} - u_{TAO}$ is 0.11 and 0.01 respectively (0.43 and 0.30 in *LMLN*). The correlations between $\overline{u}$ and u_{TAO} are greater than 0.62, largely exceeding the significant level (0.3) at the four locations. As seen in the figure, the derived velocity reproduces rather well the features of the TAO current variations during the ENSO 1997-98.

The first mode of an EOF analysis in the latitude-time domain (Fig. 8) yields a robust meridional pattern of variations at the four longitudes (explained variance $> 64\%$). The EOF profiles (top, left) match gaussian functions $y \mapsto \exp\left[-\frac{(y-l)^2}{\lambda^2}\right]$ (explained variance $> 95\%$ between 10^oN and 10^oS), with, on average, e-folding scale $\lambda \simeq 3.1^o$. Amplitudes exceed attenuation scale $(1/e)$ between 4^oN and 3^oS, and maxima are slightly moved to the north of the equator ($l \simeq 0.6^oN$), compared to symmetrical structure of equatorial trapped waves. The PCs (bottom) are very similar to the local equatorial time series, and similarly correlated to the 0^oN-TAO currents. Statistically coherent structure in the equatorial waveguide is also shown by meridional profiles of correlation between local velocity and 0^oN-TAO currents (top, right). Correlation is significantly positive (> 0.3) over $5^oN - 4.5^oS$, and negative beyond $6^oN - 6^oS$. These empirical structures of variations are consistent with those found by Delcroix et al. (1991), who analyzed the signature of equatorial Kelvin and Rossby waves in satellite *ssh* and in derived geostrophic currents. For example, they estimated a 4^o e-folding scale for an equatorial trapped wave. Note the present approach differs from Delcroix et al. (1991) and Picaut and Tournier (1991) since the estimate of continuous

velocity profiles across the equator is obtained through an orthogonal basis of polynomials which are independent of wave theory (Appendix A). This polynomial expansion procedure is notably crucial to infer the strongly sheared two-branch profile of the mean current, as well as to derive the large scale structures of the time-varying velocity.

The variations of the surface velocity involve the whole system of the equatorial currents, and throughout the 1992 to 2000 period, anomalies were most intense during the 1997-98 *El Niño-La Niña* event (Fig. 9). Broad scale reversed current replaced the SEC in 1997, whereas the SEC considerably intensified and extended westward in 1998. Also in April 1998 there was anomalous eastward flow east of 130^oW and westward flow to the west, which caused strong zonal divergence between 130^oW and 140^oW. This likely contributed to the pycnocline upwelling and rapid appearance of the cold *sst* anomaly in May 1998 described in McPhaden (1999).

4.3.2 Meridional velocity

The variations of the meridional currents at the four equatorial TAO locations are dominated by monthly and shorter timescale fluctuations (not shown). The estimated velocity has roughly the same order of magnitude but is not significantly correlated to the TAO currents ($c \sim 0.1-0.2$). Data errors and limitations inherent to the linear steady-state model probably explain the weak correlation. This is consistent with Seidel and Giese (1999) indicating that at present, altimeter data do not resolve these fluctuations.

5 Conclusion

Assuming a simple balance in the momentum equation between Coriolis acceleration, pressure gradient and vertical diffusion, we derive a diagnostic model of the surface velocity in function of *ssh* ($+dh$), $\boldsymbol{\tau}$ and *sst*. Two scalar parameters are involved that schematically characterize the vertical distribution of the velocity within the surface layer: a depth scale

H and a coefficient of vertical diffusion A. The parameter H is deduced from minimizing considerations of the mean momentum balance at the equator and from adjustment to observational data. The coefficient A is parameterized in function of the surface wind speed based on prior literature. An orthogonal polynomial expansion procedure is used to overcome the residual equatorial singularity. The velocity is inferred from de-meaned TOPEX/Poseidon *ssh*, SSM/I wind velocity and Reynolds *sst*, and is completed using Levitus *dh*. The estimated mean velocity agrees closely with the Johnson (2001) drifter field in both zonal and meridional directions. Consistently, westward biases found in *LMLN* are largely corrected. The estimated seasonal fluctuations are also in agreement with the *DRCM* climatology, and the variations of zonal velocity closely correlated with the TAO mooring surface current. For the meridional component, agreement with *DRCM* is found where seasonal fluctuation amplitude is largest (large signal-to-noise ratio), but there is no significant correlation with the TAO meridional currents on the equator.

Since the time-varying velocity is derived from the same formulations as the mean flow, local acceleration (u_t, v_t) is neglected. This assumption is seemingly reasonable considering results in sections 4.2 and 4.3. However, we note that u_t on the equator may have a magnitude comparable to the zonal pressure gradient for the seasonal cycle, but is negligible on interannual timescale (Yu and McPhaden, 1999a). Therefore the quasi-steady assumption could imply some of the discrepancy between the calculated velocity and TAO measurements on seasonal timescale.

In their study, Grodsky and Carton (2001) estimated surface currents in the tropical Pacific during the same period. A major difference between their method and ours is that their analyzed velocity includes the drifter data. Mean differences with TAO surface currents are on the same order as those found in the present study (Sec. 4.3) (they obtain smaller departure at 140^oW, $4\,cm/s$, and larger departure at 110^oW, $5\,cm/s$). Correlation coefficients between their analyzed velocity and the TAO mooring currents were not indicated, but the simple comparison between our time series in Fig. 7 and theirs (their Fig.2) shows that, at the least, our diagnostic model reproduces ocean currents with same degree of accuracy.

In summary, the new model overcomes the major limitation in the previous work by *LMLN*, namely the large inaccuracies previously noted in the cold tongue. Elsewhere the two derived current fields are nearly indistinguishable. The improvements were related to key properties of the new model: 1) introduction of vertical shear that accounts for vertical momentum diffusion, 2) introduction of a set of orthogonal polynomial basis functions to give much better accuracy of the meridional structure of the currents near the equator, and 3) introduction of a buoyancy term which accounts for vertical shear and velocity. The new surface current data will allow the next level of diagnostic and operational studies.

A Meridional structure across the equatorial area: technical aspects

As the velocity terms derived from Eq (7) are singular on the equator, the total surface velocity must be estimated using an approximation procedure. Let $[y_s, y_n]$ be the latitude range over which such an approximation is effectively considered, and let us just assume $|y_s|, |y_n| > R_o$ where $R_o \approx 2.2^o$ is the Rossby radius of deformation ($LMLN$).

In the equatorial β-plane, Eq (7) is written $iy\boldsymbol{U}_0(y) = \boldsymbol{F}(y)$, where variables are non-dimensional and $\boldsymbol{F}$ is the force term (hereafter subscript "0" of $\boldsymbol{U}_0$ is omitted). Since the following method is linear, $\boldsymbol{F}$ denotes either one single contributory force or the summation of all the forces in r.h.s of (7). The "raw" solution is defined by $\boldsymbol{U}_{raw} \equiv \frac{\boldsymbol{F}}{iy}$. It is singular on the equator when $\boldsymbol{F}(0) \neq 0$, but is the exact regular solution when $\boldsymbol{F}(0) = 0$. The sought velocity $\boldsymbol{U}$ is approximated by a series expansion of real functions $\Phi_k(y)$ with complex coefficients $\boldsymbol{a}_k$, $k = 0, \cdots, M-1$:

$$\boldsymbol{U}(y) \approx \boldsymbol{U}_a(y) \equiv \sum_{k=0}^{M-1} \boldsymbol{a}_k \Phi_k(y), \;\; y_s \leq y \leq y_n \tag{12}$$

A new formulation of the problem is then: finding $\boldsymbol{U}_a(y)$, such that $\int_{y_s}^{y_n} |iy\boldsymbol{U}_a - \boldsymbol{F}|^2 dy$ is minimum. If the functions $\Phi_k(y)$ are orthogonal and normalized in the sense that

$$\int_{y_s}^{y_n} \Phi_k(y)\Phi_l(y)y^2 dy = 0 \;\text{ if } k \neq l \tag{13a}$$

$$= 1 \;\text{ if } k = l, \tag{13b}$$

then the coefficients $\boldsymbol{a}_k$, $k = 0, \cdots, M-1$, are simply given by the integral:

$$\boldsymbol{a}_k = -i \int_{y_s}^{y_n} \boldsymbol{F}(y)\Phi_k(y) y dy \tag{14}$$

Polynomials $\Phi_k(y)$ verifying (13) are determined using an orthogonalization procedure (e.g. Courant and Hilbert, 1953) and the first seven polynomials are shown in Fig. 10. This polynomial set is complete, thus any function that is smooth enough can be expanded in a series of polynomials $\Phi_k(y)$.

In practice $\boldsymbol{F}$ is given at a discrete set of latitudes, and the adjustment of M depends on the grid step Δy, the boundaries y_s and y_n and the latitude number N_y. A first condition ensures that the solution is exact in the regular case: M must be large enough, such that when $\boldsymbol{F}(0) = 0$ (no singularity), $\boldsymbol{U}_a(y) = \boldsymbol{U}_{raw}(y)$. A second condition requires that on the equator the solution is identical to the β-plane solution:

$$\boldsymbol{U}_a(0) = \boldsymbol{U}^{(\beta)}(0) \equiv \frac{1}{i}\frac{\partial \boldsymbol{F}}{\partial y}(0) \tag{15}$$

Note that $\boldsymbol{U}^{(\beta)}(0)$ is the general expression of (9). The condition (15) is also satisfied for large enough M. Performing various tests based on theoretical functions as well as simulated and real data, we found that $M \approx 0.75 \times N_y$ is appropriate to satisfy the above requirements when $\Delta y = 1^o$ (the effective step in this study). Fig 2 shows meridional profiles of $\boldsymbol{U}_a$ for the mean flow. Since we choose $y_n = -y_s = 8^o$, the polynomial number is $M \approx 12$. The transition from $\boldsymbol{U}_a$ to $\boldsymbol{U}_{raw}$ is accomplished between 5^o and 8^o through a simple linear weighing function.

B Characteristics of the wind-driven velocity

B.1 Comparison with the Ekman model

The wind-driven velocity $\boldsymbol{U}_\tau$ deduced from (6) and (7) and used in the present study to estimate the surface currents was first established by Stommel (1960). Letting $z = 0$ for simplicity, it is given by $\boldsymbol{U}_{\tau 0} = \frac{1}{\tanh\left(\frac{H}{\hbar_e}\right)}\frac{\hbar_e \boldsymbol{\tau}}{A}$, and is the effect of vertical diffusion of wind stress from surface to deeper levels in function of a vertically constant viscosity parameter A. It is therefore similar in principle to the classic Ekman model (here also written for $z = 0$), $\boldsymbol{U}_{ek0} = \frac{\hbar_e \boldsymbol{\tau}}{A}$. The equations leading to Stommel and Ekman models and their boundary conditions at the surface are identical, but conditions at deeper levels are different. In the Ekman model the velocity is required to be bounded at infinite depth, whereas in the Stommel model, the shear must be zero at a certain level H. The two models are

indistinguishable far enough from the equator but differ significantly when approaching the equator. Using $f = \beta y$, a latitudinal scale is given by $y_r = \frac{2A}{\beta h^2}$ (satisfying $\frac{y}{y_r} = \left(\frac{h}{h_e}\right)^2$), and for $h = 30\,m$ and $A = 30\,cm^2/s$, y_r is 2.6^o, hence on the order of the Rossby radius of deformation. For decreasing latitudes, the amplitude of the velocities grows infinitely, the Stommel model increasing at a higher rate. Indeed, the Stommel velocity is asymptotically proportional to $1/f$ when $f \to 0$ and the Ekman velocity to $1/f^{1/2}$. Due to this asymptotical property, the term $f\boldsymbol{U}_{\tau 0}$ and not $f\boldsymbol{U}_{ek0}$ combines naturally with the geostrophic term $f\boldsymbol{U}_{\zeta}$ in (7) to yield the balance condition (8) and to compose the total velocity.

B.2 Meridional profile across the equator

We estimate the term $\boldsymbol{U}_\tau(y,z)$ produced by a constant zonal and meridional wind stress (Fig 11). With the standard value $U_* \simeq 6 \times 10^{-3}\,m/s$ (wind speed on the order of $5\,m/s$), the wind-driven contribution is about $10\,cm/s$. The velocity vectors $\boldsymbol{U}_\tau(-15m)$ and $\overline{\boldsymbol{U}_\tau}$ have similar magnitude and angles, and this is consistent with *LMLN* who found a layer thickness $h = 32.5\,m$ characteristic of the $15\,m$-depth drifter velocity. Note however that the velocity magnitude at $z = 0$ is two to three times larger than $|\overline{\boldsymbol{U}_\tau}|$ or $|\boldsymbol{U}_\tau(-15m)|$. In *LMLN* the peak amplitude on the equator is $\sim 4650\,s\,m^{-1}$ (their Figs 4 and 5) versus about $3000\,s\,m^{-1}$ for the $0-30\,m$ average in Fig 11. This difference occurs because *LMLN* assumed all of the dissipation was absorbed in the layer depth h, as a slab over a motionless layer below. This is unrealistic on the equator considering the results given here. In the presence of mean westward trade winds, this reduction (per unit wind stress) of about 36% mitigates a significant fraction of the westward surface current bias obtained by *LMLN* in the cold tongue.

References

Atlas, R., R. Hoffman, S. Bloom, J. Jusem, and J. Ardizzone, 1996: A multi-year global surface wind velocity data set using ssm/i wind observations. *Bulletin of American Meteorological Society*, **77**, 869–882.

Bonjean, F., 2001: Influence of surface currents on the sea surface temperature in the tropical pacific. *J. Phys. Oceanogr.*, **31**, 943–961.

Courant, R. and D. Hilbert, 1953: *Method of Mathematical Physics*, vol. 1. Wiley Classics Edition.

Delcroix, T., J. Picaut, and G. Eldin, 1991: Equatorial kelvin and rossby waves evidenced in the pacific ocean through geosat sea level and surface current anomalies. *J. Geophys. Res.*, **96**, 3249–3262.

Delcroix, T and J. Picaut, 1998: Zonal displacement of the western equatorial pacific fresh pool. *J. Geophys. Res.*, **103**, 1,087–18,1,098.

Frankignoul, C., F. Bonjean, and G. Reverdin, 1996: Interannual variability of surface currents in the tropical pacific during 1987-1993. *J. Geophys. Res.*, **101**, 3,629–3,647.

Grodsky, S.A. and J.A. Carton, 2001: Intense surface currents in the tropical pacific during 1996-1998. *J. Geophys. Res.*, **106**, 16,673–16,684.

Johnson, G. C, 2001: The pacific ocean subtropical cell surface limb. *Geophysical Research Letters*, **28**, 1,771–1,774.

Lagerloef, G.S.E., G.T. Mitchum, R. Lukas, and P.P. Niiler, 1999: Tropical pacific near surface currents estimated from altimeter, wind and drifter data. *J. Geophys. Res.*, **104**, 23,313–23,326.

Large, W.G. and S. Pond, 1981: Open ocean momentum flux measurements in moderate to strong winds. *J. Phys. Oceanogr.*, **11**, 324–336.

Levitus, S., R. Burgett, and T.P. Boyer, 1994: World ocean atlas 1994 vol.3: Salinity. Noaa

atlas nesdis 3, 111 pp., NOAA, Dept. of Commerce, Washington, D.C.

——— and T.P. Boyer, 1994: World ocean atlas 1994 vol.4: Temperature. Noaa atlas nesdis 4, 117 pp., NOAA, Dept. of Commerce, Washington, D.C.

McPhaden, M.J., 1999: Genesis and evolution of the 1997-98 el nino. *Science*, **283**, 950–954.

Philander, S.G.H. and R.C. Pacanowski, 1980: The generation of equatorial currents. *J. Geophys. Res.*, **85**, 1,123–1,136.

Picaut, J. and R. Tournier, 1991: Monitoring the 1979-1985 equatorial pacific current transports with expendable bathythermograph data. *J. Geophys. Res.*, **96**, 3263–3277.

———, M. Ioualalen, C.Menkes, T. Delcroix, and M.J. McPhaden, 1996: Mechanism of the zonal displacements of the pacific warm pool: Implications for enso. *Science*, **274**, 1,486–18,1,489.

Ralph, E.A. and P.P. Niiler, 1999: Wind-driven currents in the tropical pacific. *J. Phys. Oceanogr.*, **29**, 2121–2129.

Reverdin, G., C. Frankignoul, E. Kestenare, and M.J. McPhaden, 1994: Seasonal variability in the surface currents of the equatorial pacific. *J. Geophys. Res.*, **99**, 20,323–20,344.

Reynolds, R.W. and T.M. Smith, 1994: Improved global sea surface temperature analyses using optimum interpolation. *J. Clim.*, **7**, 929–948.

Santiago-Mandujano, F. and E. Firing, 1990: Mixed-layer shear generated by wind stress in the central equatorial pacific. *J. Phys. Oceanogr.*, **20**, 1576–1582.

Seidel, H.F. and B.S. Giese, 1999a: Equatorial currents in the pacific ocean 1992-1997. *J. Phys. Oceanogr.*, **104**, 7849–7863.

——— and B.S. Giese, 1999b: Equatorial currents in the pacific ocean 1992-1997. *J. Geophys. Res.*, **104**, 7,849–7,863.

Stommel, H., 1960: Wind-drift near the equator. *Deep Sea Research*, **6**, 298–302.

Yu, X. and M.J. McPhaden, 1999a: Dynamical analysis of seasonal and interannual vari-

ability in the equatorial pacific. *J. Phys. Oceanogr.*, **29**, 2,350–2,369.

——— and M.J. McPhaden, 1999b: Seasonal variability in the equatorial pacific. *J. Phys. Oceanogr.*, **29**, 925–947.

Captions

Fig 1: (Top) Derivative with respect to H of the equatorial momentum residual (see text) for the zonal and meridional components, using $\boldsymbol{\tau}$, dh and sst data. (Bottom) Derivative with respect to H of the standard deviation of difference between the modeled velocity and: (thick line) the mean field from drifters in the whole basin, (thin lines) the $10\,m$-depth TAO current data at 0^oN 165^oE, 170^oW, 140^oW and 110^oW.

Fig 2: Momentum balance from observations along the equator in the Pacific. The depth scale H is equal to $70\,m$. Contributions are derived from: (Continuous thick line) $\boldsymbol{\tau}$, (continuous line) dh gradient, (dashed line) sst gradient. Dotted line is the sum of contributions. To emphasize the basin scale, each term is fitted to a 5-degree polynomial in longitude.

Fig 3: Mean velocity: (1st panel) diagnostic velocity relative to the $30\,m$-depth surface layer, from dh, $\boldsymbol{\tau}$ and sst data. (2nd panel) $15\,m$-Velocity from drifters. (3rd panel) diagnostic velocity relative to the $30\,m$-depth surface layer, using the GCM-simulated fields dh, $\boldsymbol{\tau}$ and sst. (4th panel) GCM-simulated velocity relative to the $30\,m$-depth surface layer.

Fig 4: Surface layer velocity from the diagnostic model using observations, in function of latitude and averaged between 140^oW and 100^oW. (Top) Zonal velocity, (Bottom) meridional velocity. (Right panels) In legend order, the three velocity terms (see text), and the drifter velocity. (Left panels) In legend order, sum of the three velocity terms, drifter velocity, and $LMLN$ velocity.

Fig 5: Seasonal cycle of the surface layer velocity, relative to the 1993-1996 and 1999 periods, for January, April, July and October.

Fig 6: (De-meaned) Seasonal fluctuations of the estimated surface layer velocity and of the surface currents from $DRCM$, in function of time and longitude. (Top) Zonal velocity on the equator ($2^oN - 2^oS$), (middle) zonal velocity between 5^oN and 12^oN, (bottom) meridional velocity between 5^oN and 12^oN. Gray shading indicates westward or southward flow. To emphasize the large scales, both fields are zonally filtered using a 10^o-gaussian

filter.

Fig 7: Variations of surface zonal currents at the four equatorial TOGA/TAO locations: from top to bottom, 165^oE, 170^oW, 140^oW and 110^oW. The thin curves represent the TAO data at $10\,m$, and the thick curves the estimated velocity. Time resolution is 10 days. For each location the correlation coefficient (c) is indicated. Significant correlation level is at most 0.3 at the four locations.

Fig 8: (top left) First-mode normalized EOFs of the estimated zonal velocity calculated in the latitude/time domain at the four longitudes 165^oE, 170^oW, 140^oW and 110^oW. Numbers in brackets are the percentage of variance explained by first mode, and vertical dash-dotted line indicates mean e-folding scale ($\simeq 0.4$). (bottom) Corresponding PCs in m/s (thick lines), and $10\,m$-depth zonal current from TAO moorings at 0^oN (thin line). c_{TAO} is the correlation coefficient between PCs and TAO currents. (top right) Correlation in function of latitude between the estimated zonal velocity and the zonal current from the TAO moorings at 0^oN. The significant level of correlation is ~ 0.3 (dash-dotted line).

Fig 9: Anomalies of the estimated velocity during four monthly periods of the 1997-98 *El Niño-La Niña* event: June 1997, November 1997, April 1998 and May 1998.

Fig 10: First seven orthogonal polynomials of the series used to approximate the near-equatorial velocity. The latitude is divided by the Rossby radius of deformation $Ro \approx 2.2^o$. Latitude range is here symmetrical with respect to the equator, and the boundaries are fixed to $\pm 8^o$ ($y_n = |y_s| \approx 3.5$).

Fig 11: Wind driven velocity contribution produced by westward wind (upper panels) and northward wind (lower panels), in function of latitude, at the depth levels 0, $-15\,m$ and $-30\,m$, and for the $30\,m$-depth surface layer. The velocity magnitude is divided by $U_*^2 \equiv |\tau_0|/\rho_m$. The arrow length indicates the amplitude and the scale is shown in bottom panel. The arrow angle indicates the velocity direction within the basin.

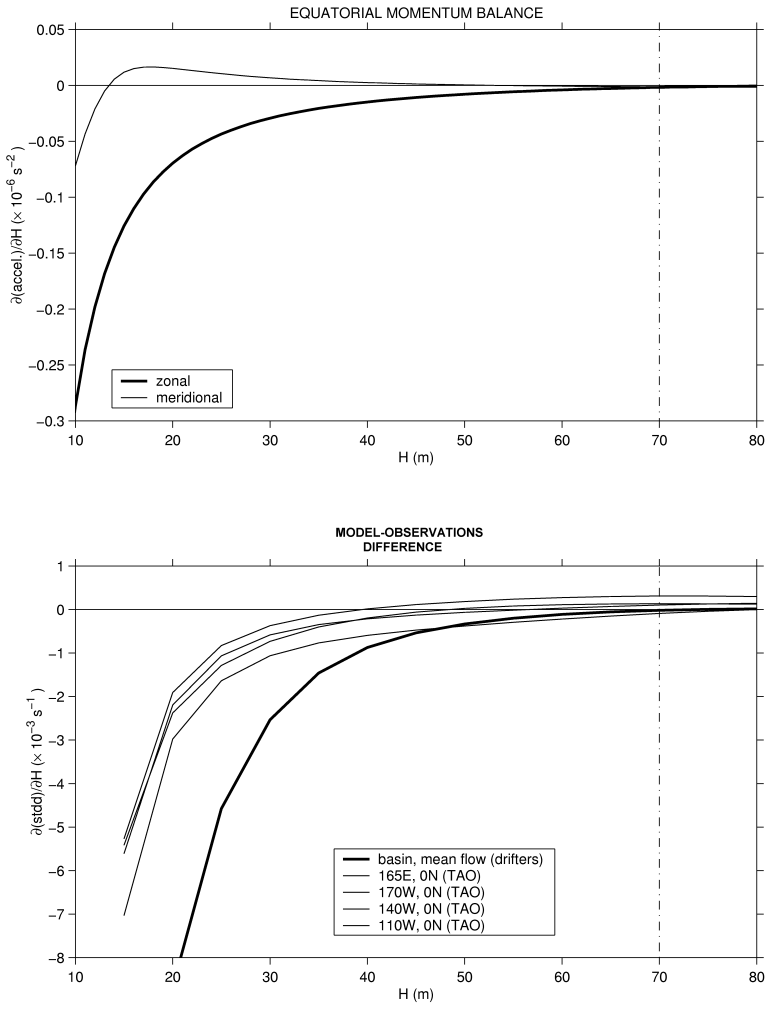
EQUATORIAL MOMENTUM BALANCE
0.05
0
−0.05
−0.1
−0.15
−0.2
−0.25
−0.3
∂(accel.)/∂H (× 10^−6 s^−2)
zonal
meridional
10
20
30
40
50
60
70
80
H (m)
MODEL-OBSERVATIONS
DIFFERENCE
1
0
−1
−2
−3
−4
−5
−6
−7
−8
∂(stdd)/∂H (× 10^−3 s^−1)
basin, mean flow (drifters)
165E, 0N (TAO)
170W, 0N (TAO)
140W, 0N (TAO)
110W, 0N (TAO)
10
20
30
40
50
60
70
80
H (m)

Figure 1:

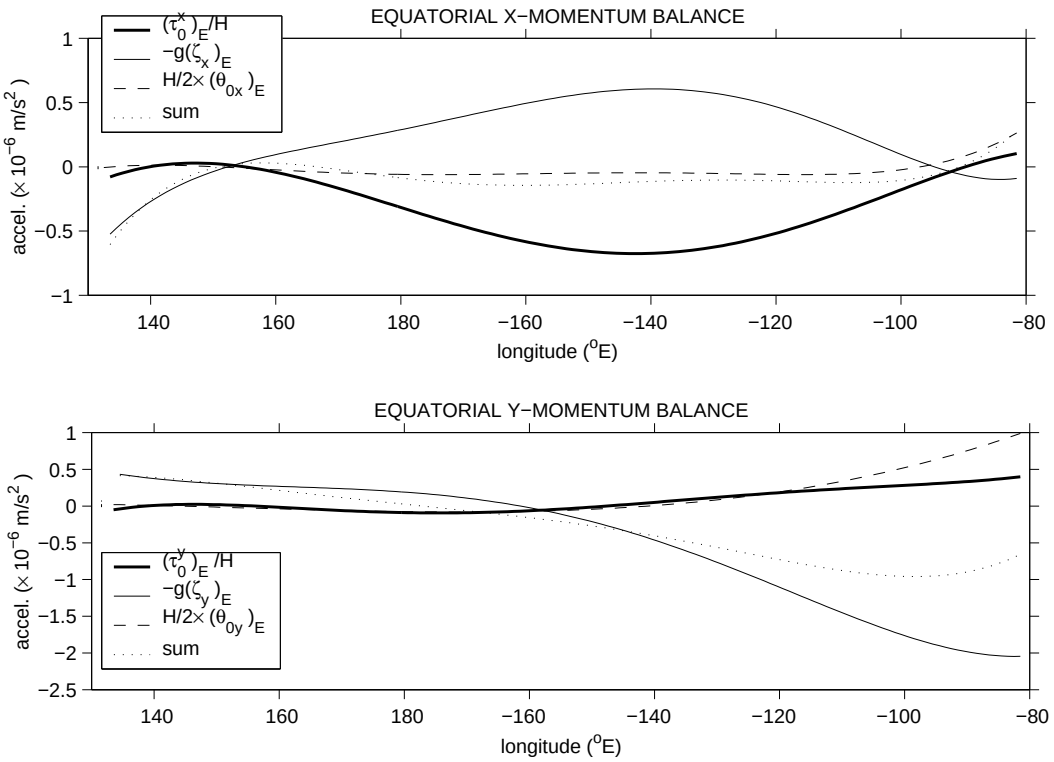
EQUATORIAL X−MOMENTUM BALANCE
$(\tau_0^x)_E/H$
$-g(\zeta_x)_E$
$H/2\times(\theta_{0x})_E$
sum
accel. ($\times 10^{-6}$ m/s^2)
longitude (^{o}E)
EQUATORIAL Y−MOMENTUM BALANCE
$(\tau_0^y)_E/H$
$-g(\zeta_y)_E$
$H/2\times(\theta_{0y})_E$
sum
accel. ($\times 10^{-6}$ m/s^2)
longitude (^{o}E)

Figure 2:

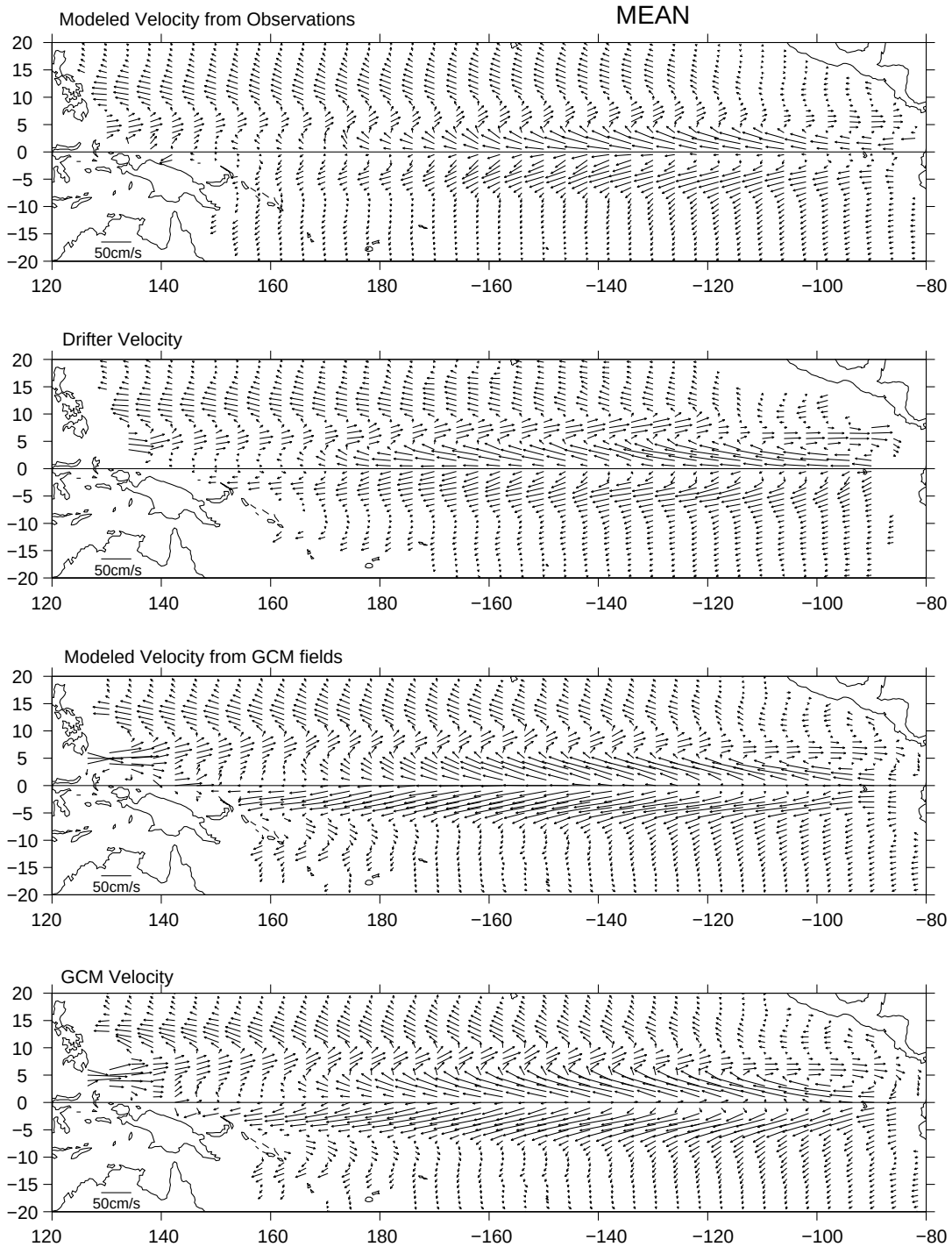
Modeled Velocity from Observations
MEAN
Drifter Velocity
Modeled Velocity from GCM fields
GCM Velocity
50cm/s
20
15
10
5
0
−5
−10
−15
−20
120
140
160
180
−160
−140
−120
−100
−80

Figure 3:

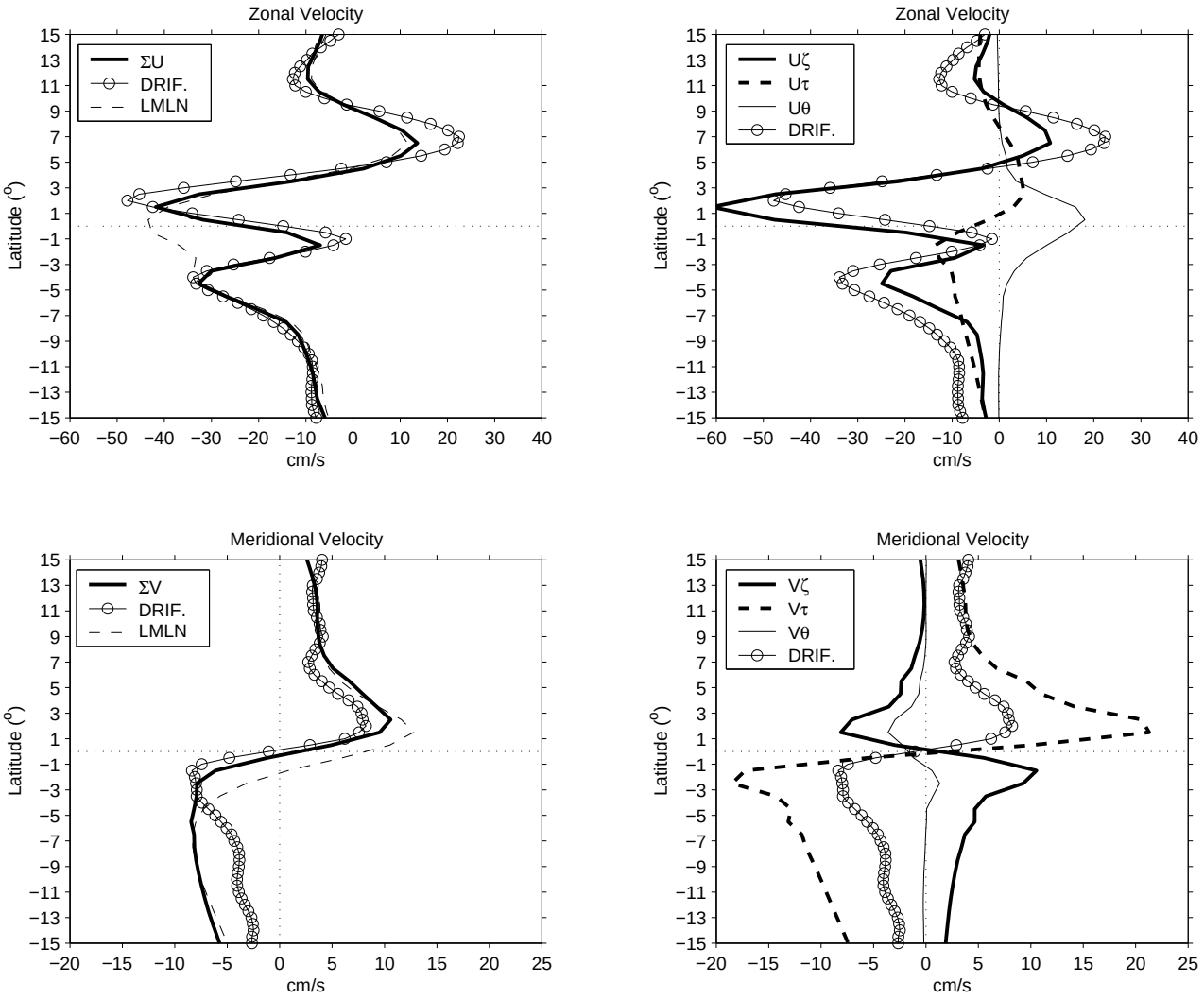
Zonal Velocity
ΣU
DRIF.
LMLN
Latitude (°)
cm/s
Zonal Velocity
Uζ
Uτ
Uθ
DRIF.
Latitude (°)
cm/s
Meridional Velocity
ΣV
DRIF.
LMLN
Latitude (°)
cm/s
Meridional Velocity
Vζ
Vτ
Vθ
DRIF.
Latitude (°)
cm/s

Figure 4:

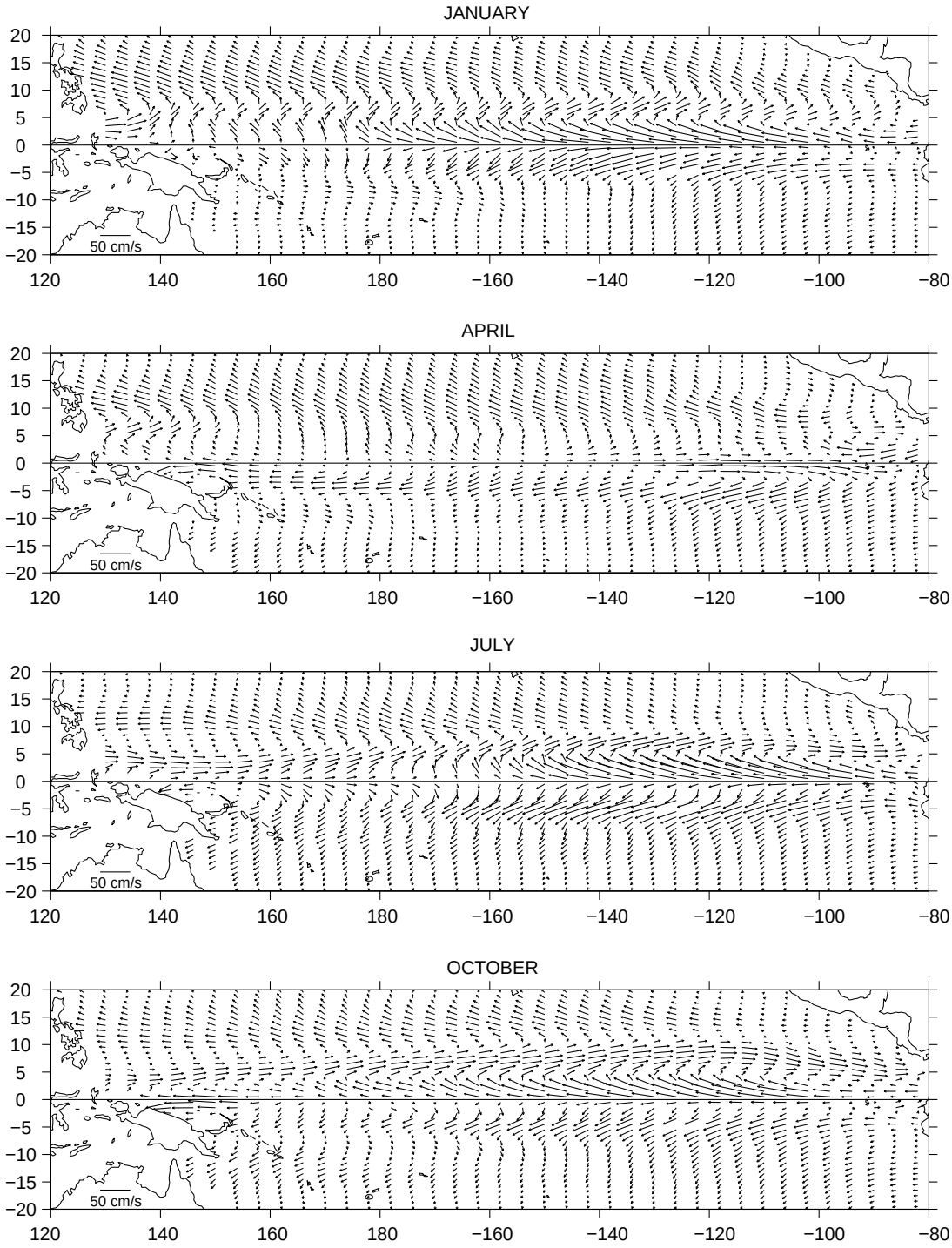
JANUARY
APRIL
JULY
OCTOBER
20
15
10
5
0
−5
−10
−15
−20
50 cm/s
120
140
160
180
−160
−140
−120
−100
−80

Figure 5:

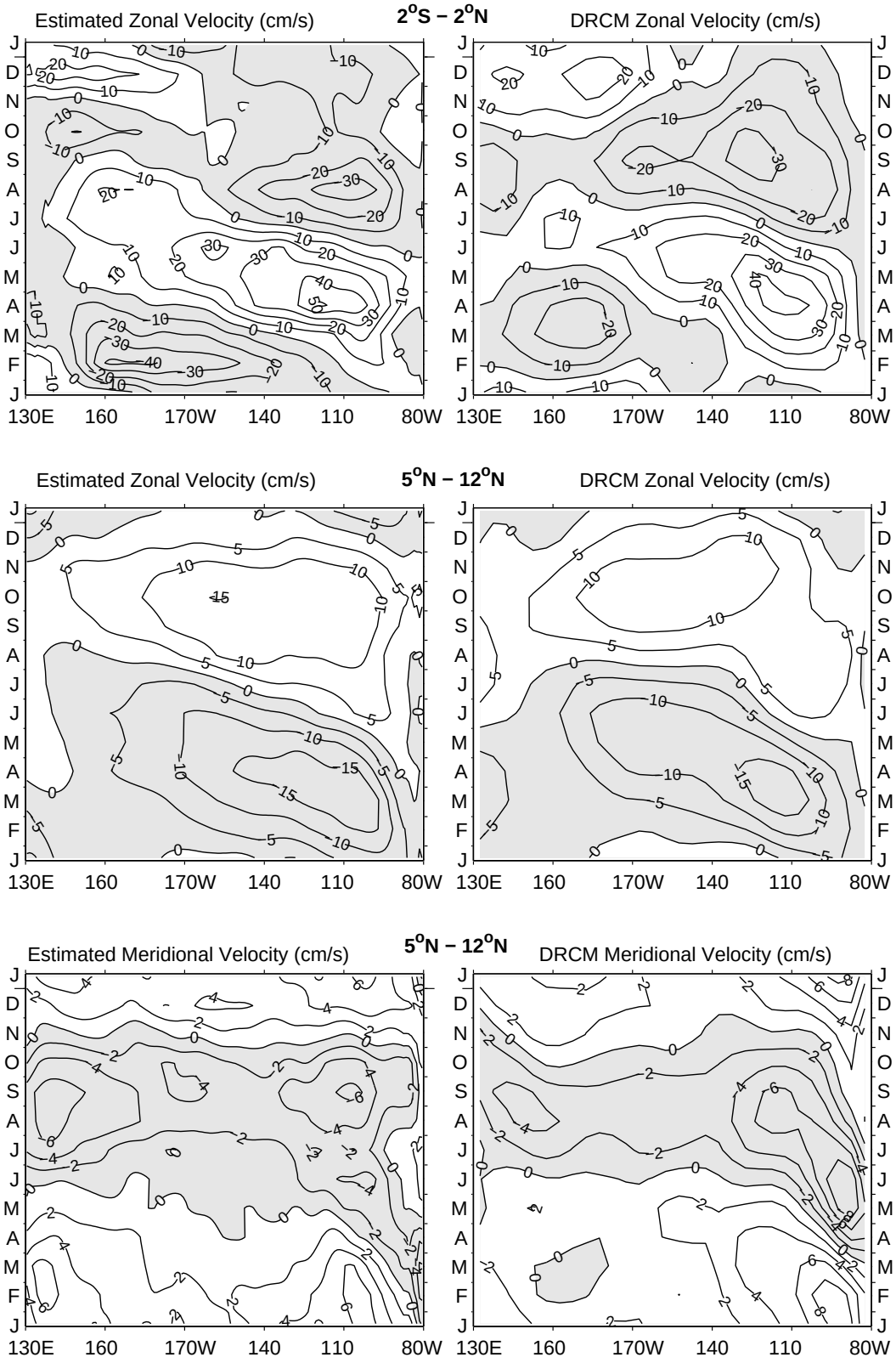
Estimated Zonal Velocity (cm/s)
2°S – 2°N
DRCM Zonal Velocity (cm/s)
Estimated Zonal Velocity (cm/s)
5°N – 12°N
DRCM Zonal Velocity (cm/s)
Estimated Meridional Velocity (cm/s)
5°N – 12°N
DRCM Meridional Velocity (cm/s)
J D N O S A J J M A M F J
130E 160 170W 140 110 80W

Figure 6:

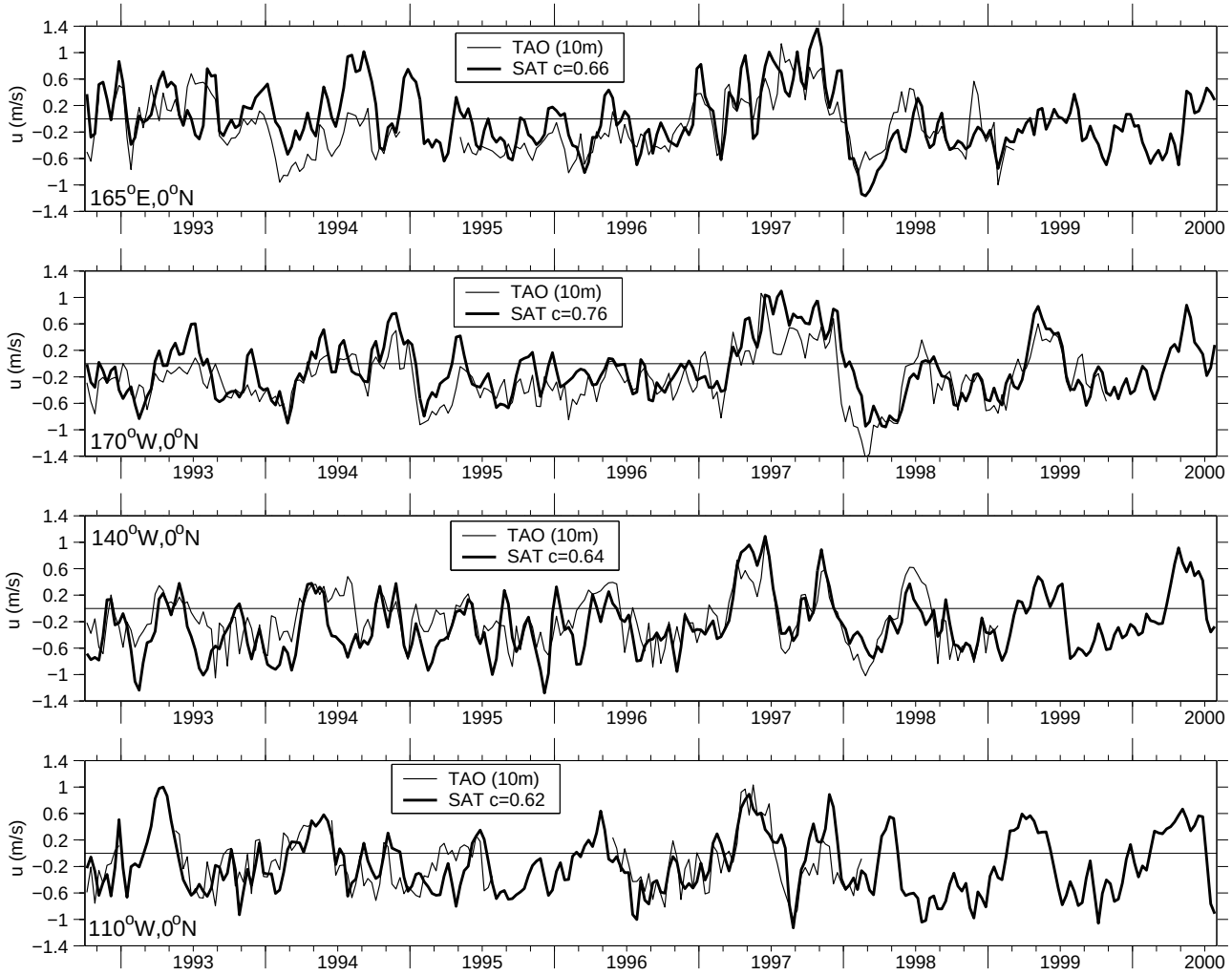
TAO (10m)
SAT c=0.66
165°E,0°N
TAO (10m)
SAT c=0.76
170°W,0°N
140°W,0°N
TAO (10m)
SAT c=0.64
TAO (10m)
SAT c=0.62
110°W,0°N
u (m/s)
1.4
1
0.6
0.2
−0.2
−0.6
−1
−1.4
1993
1994
1995
1996
1997
1998
1999
2000

Figure 7:

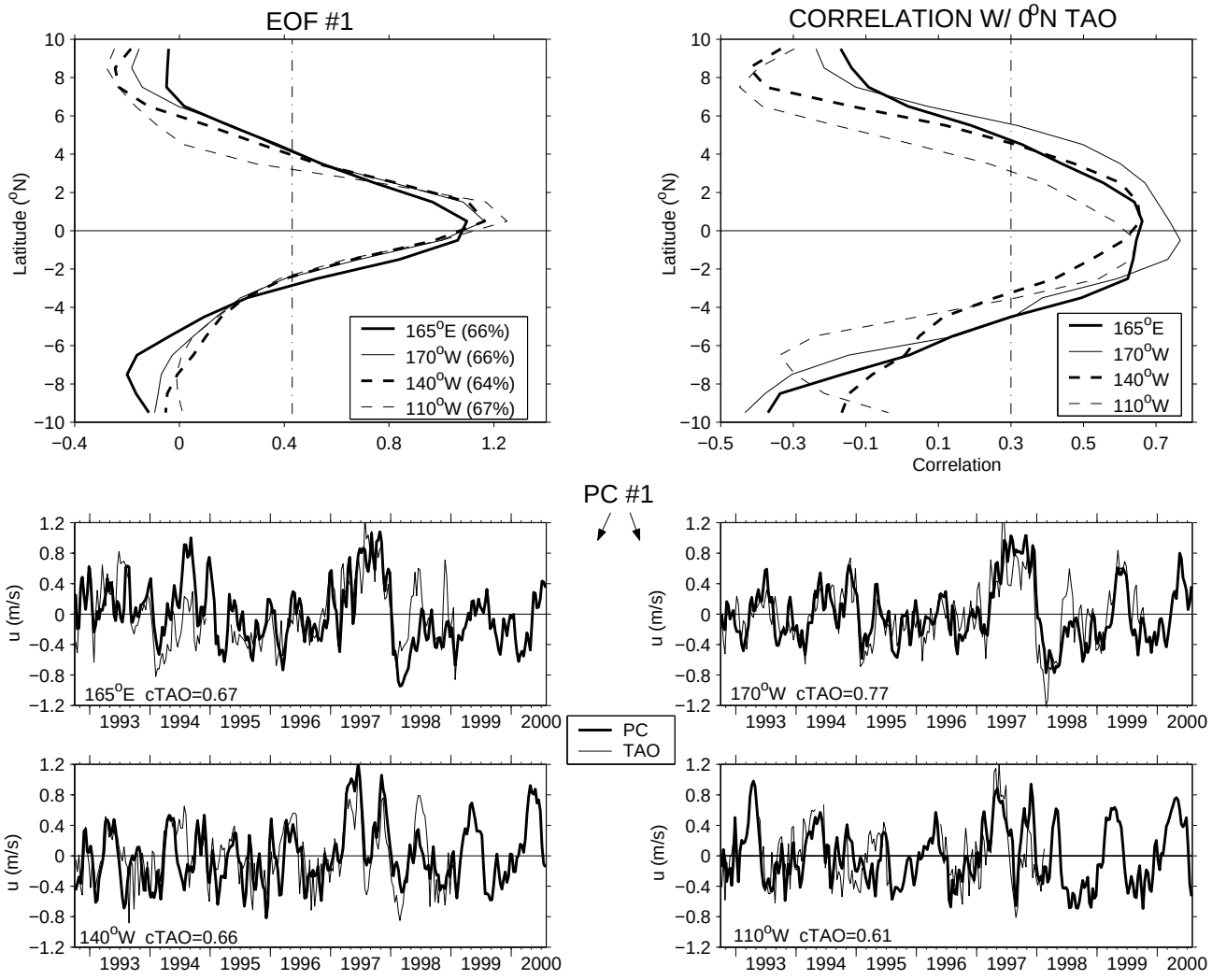
EOF #1
CORRELATION W/ 0°N TAO
Latitude (°N)
Correlation
165°E (66%)
170°W (66%)
140°W (64%)
110°W (67%)
165°E
170°W
140°W
110°W
PC #1
u (m/s)
165°E cTAO=0.67
170°W cTAO=0.77
140°W cTAO=0.66
110°W cTAO=0.61
PC
TAO

Figure 8:

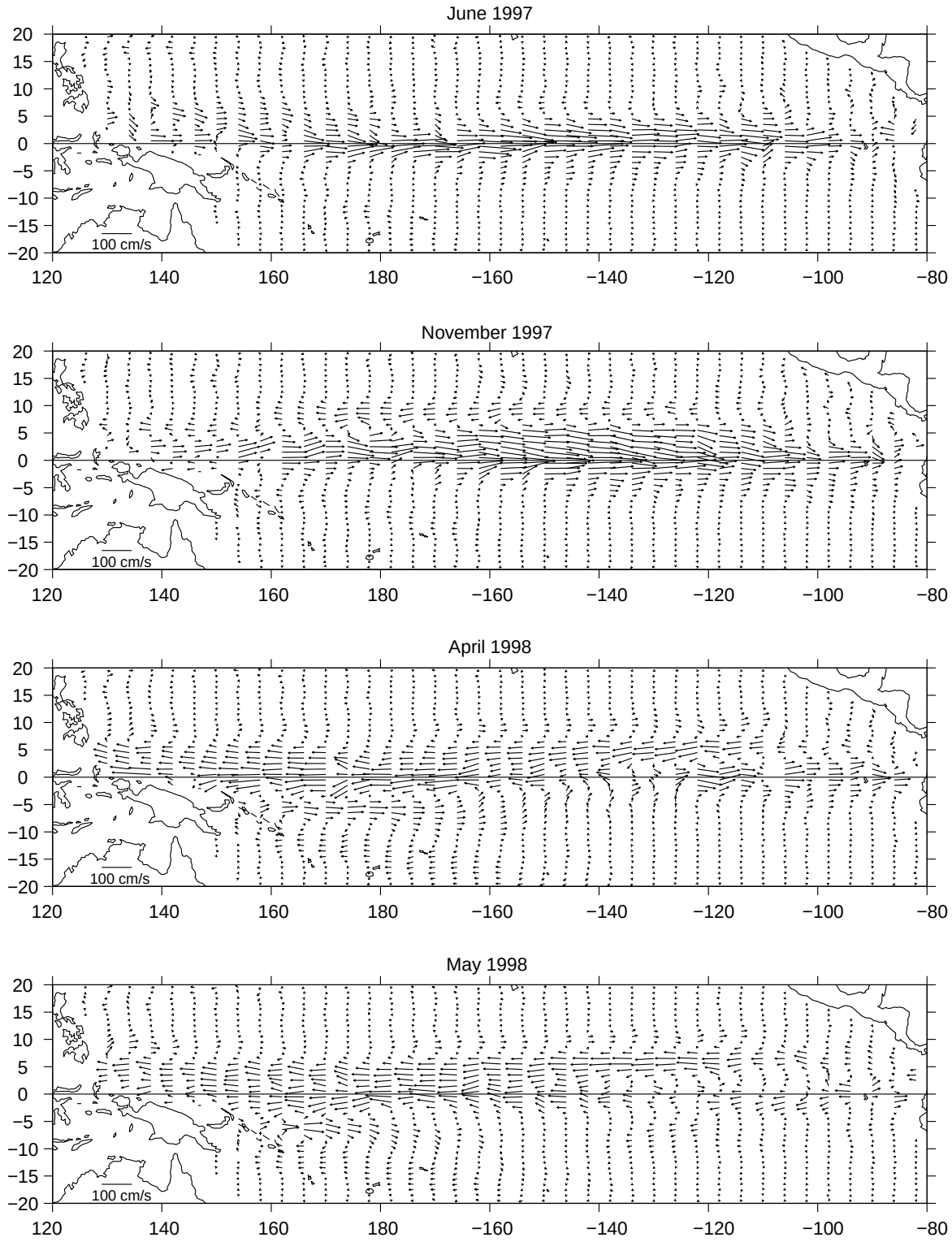
June 1997
November 1997
April 1998
May 1998
100 cm/s
20
15
10
5
0
−5
−10
−15
−20
120
140
160
180
−160
−140
−120
−100
−80

Figure 9:

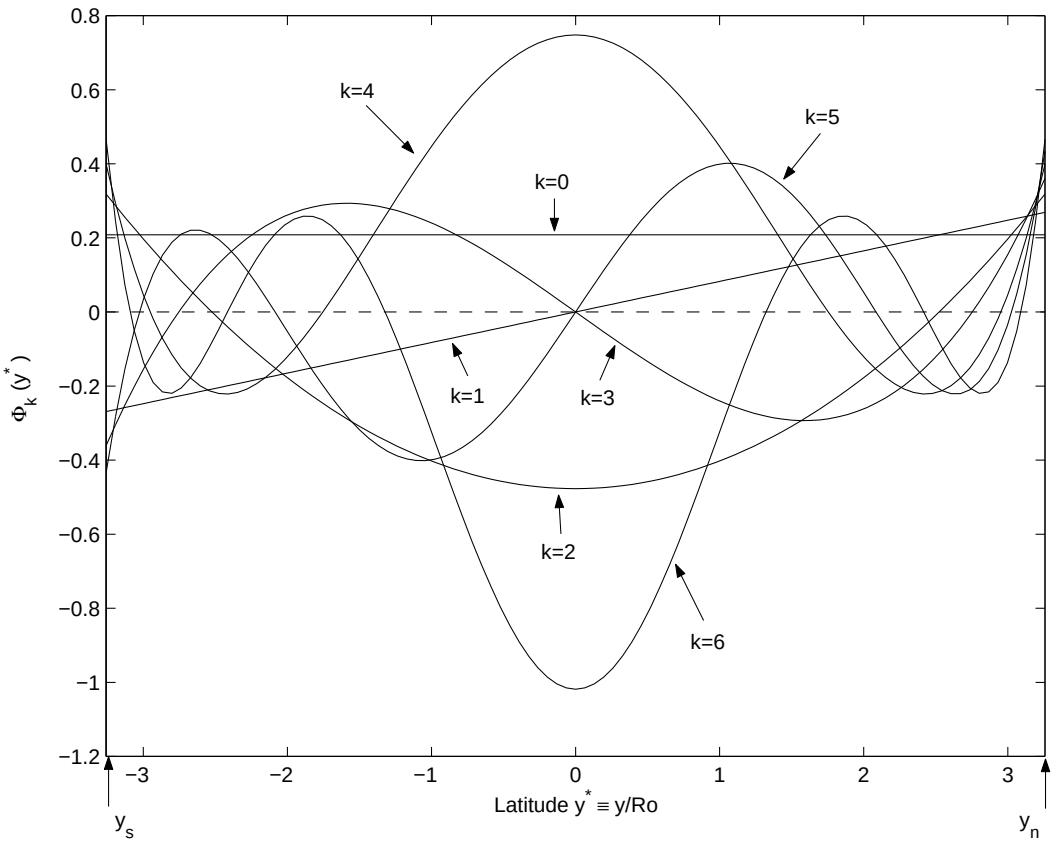
0.8
0.6
0.4
0.2
0
−0.2
−0.4
−0.6
−0.8
−1
−1.2
−3
−2
−1
0
1
2
3
k=4
k=5
k=0
k=1
k=3
k=2
k=6
$\Phi_k(y^*)$
Latitude $y^* \equiv y/Ro$
y_s
y_n

Figure 10:

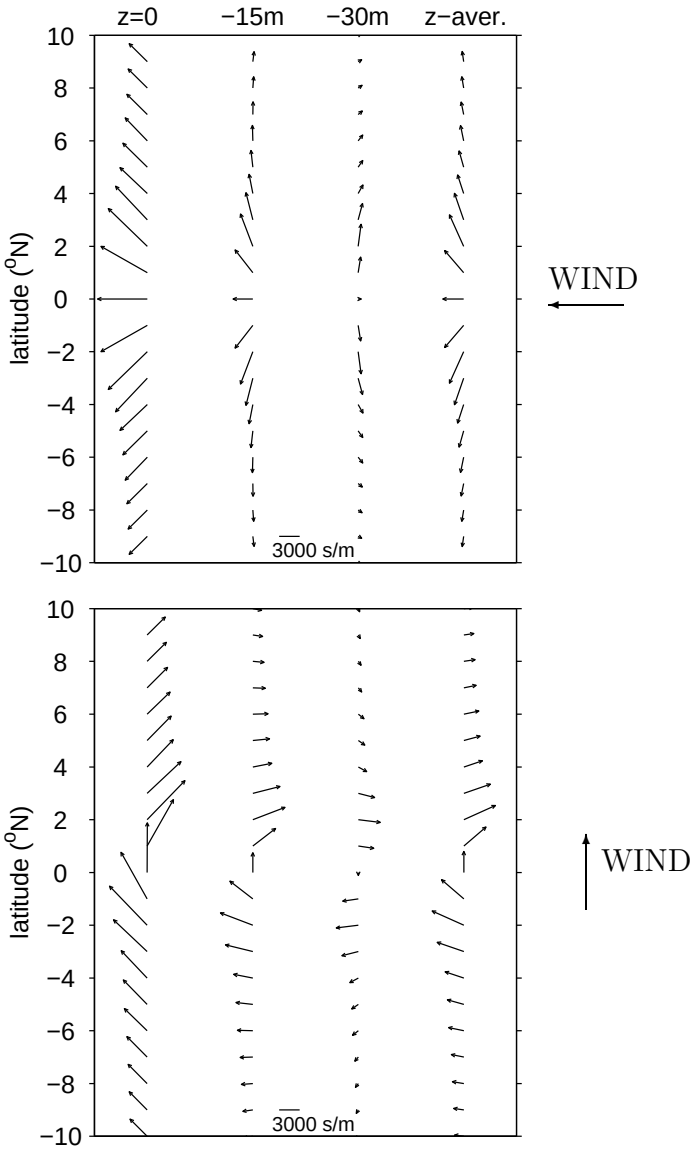
z=0
−15m
−30m
z−aver.
latitude (°N)
10
8
6
4
2
0
−2
−4
−6
−8
−10
3000 s/m
WIND
latitude (°N)
10
8
6
4
2
0
−2
−4
−6
−8
−10
3000 s/m
WIND

Figure 11: